

Kane Fermion in a Two-Dimensional π -Conjugated Bis(iminothiolato)nickel Monolayer

Aizhu Wang,^{†,‡,§,||} Xinrui Zhao,[§] Mingwen Zhao,^{*,†,¶} Xiaoming Zhang,[†] Yuanping Feng,^{*,||} and Feng Liu^{§,#}

[†]School of Physics and State Key Laboratory of Crystal Materials, Shandong University, Jinan, 250100, Shandong, China

[‡]Department of Electrical and Computer Engineering & Department of Physics, National University of Singapore, Singapore, 117579, Singapore

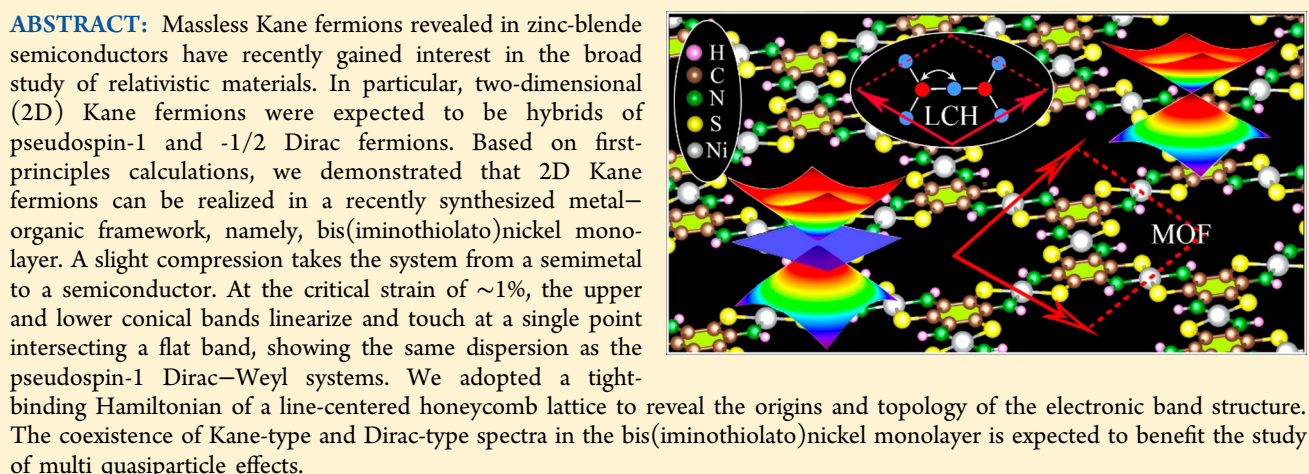
[§]School of the Gifted Young, University of Science and Technology of China, Hefei, 230026, Anhui, China

[¶]Department of Physics & Centre for Advanced Two-dimensional Materials, National University of Singapore, Singapore, 117542, Singapore

^{||}Department of Materials Science and Engineering, University of Utah, Salt Lake City, Utah 84112, United States

[#]Collaborative Innovation Center of Quantum Matter, Beijing, 100084, Beijing, China

Supporting Information



Low-energy quasiparticles in condensed matter systems that arise from the interaction of electrons with a periodic crystal potential offer an economical approach to mimic the relativistic particles in high-energy physics. For example, the electrons in graphene behave as two-dimensional (2D) massless Fermions that obey the Dirac equation due to the gapless conical bands.¹ This concept has been demonstrated in topological materials such as topological insulators,^{2–4} Weyl and Dirac semimetals,^{5–7} thanks to the unique electronic band structures of the materials. The exotic properties of the condensed matter analogues of high-energy relativistic particles revealed in these materials open an avenue for novel electronic devices.

Recently, a new quasiparticle, namely, three-dimensional (3D) massless Kane fermion, has been discovered in $Hg_{1-x}Cd_xTe$ ^{8,9} and Cd_3As_2 ¹⁰ based on their energy dispersion relation featuring cones crossed at the vertex by an additional flat band. Interestingly, the band gap and the electronic dispersion in $Hg_{1-x}Cd_xTe$ can be tuned intrinsically by adjusting the chemical composition, leading to an inverted-to-

normal band structure topological transition existing at the critical cadmium concentration of $x \sim 0.17$.⁸ Theoretical works showed that a tunable gap parameter (E_g) in the low-energy Kane model takes the system from a semiconductor ($E_g > 0$) to a semimetal ($E_g < 0$).¹¹ At the critical value $E_g = 0$, the upper and lower cones linearize and touch at a single point intersecting a flat band, showing the same dispersion as the pseudospin-1 Weyl semimetal.^{12,13} Although 3D massless Kane fermions share many features with Weyl and Dirac fermions, i.e., optical absorption that is linear in frequency, Landau levels, and their Zeeman splitting, which are proportional to $B^{1/2}$ and rigidly related to each other, their inequivalence in spin and orbital splitting open further perspectives for its uses in electronic devices.^{8,9}

More interestingly, theoretical works^{14,15} showed that the 2D Kane model maps onto an intermediate value ($\alpha = 1/\sqrt{3}$) of

Received: November 13, 2017

Accepted: January 17, 2018

Published: January 17, 2018



the α -T₃ model,¹⁶ which interpolates between the pseudospin-1/2 ($\alpha = 0$) and pseudospin-1 ($\alpha = 1$) Dirac–Weyl systems. The intermediate value of α leads to non- π -quantized Berry phases of the two conical bands ($\pi/2$).^{14,15} The 2D Kane Fermion can therefore be regarded as a hybrid of pseudospin-1 and -1/2 Dirac fermions with usual magneto-optical conductivity. However, a 2D Kane fermion has not yet been realized in experiments due to the lack of candidate materials.

Here, based on first-principles calculations, we demonstrated that a recently synthesized metal–organic framework (MOF), namely, bis(iminothiolato)nickel monolayer,¹⁷ can host 2D Kane fermions. The conical bands and the flat band of the 2D MOF can be tuned by external strain, equivalent to a tunable gap parameter (E_g) in the low-energy Kane model.^{11–13} At the critical compressive strain of $\sim 1\%$, the upper and lower conical bands linearize and touch at a single point intersecting a flat band, showing the same dispersion as the pseudospin-1 Dirac–Weyl systems. We also proposed a tight-binding (TB) Hamiltonian of a line-centered honeycomb (LCH) lattice to reveal the origins and topology of the electronic band structure. Our work offers the first candidate material for realization of 2D massless Kane fermions and thus is expected to motivate the following experimental exploration.

Crystal and Electronic Structures. 2D MOFs consisting of transition metal atoms and organic ligands have diverse forms with intriguing properties.^{18–24} In a recent experiment, a π -conjugated coordination nanosheet comprising bis(iminothiolato)nickel moieties with 2D-planar structures was synthesized by a reaction of Ni²⁺ with 1,3,5-triaminobenzene-2,4,6-trithiol in the presence of ferrocenium ion.¹⁷ Bis(iminothiolato)nickel monolayer can be naturally produced through exfoliation of the nanosheet (see Supporting Information). The optimized configuration of the bis(iminothiolato)nickel ($\text{Ni}_3\text{C}_{12}(\text{NH})_6\text{S}_6$) monolayer is shown in Figure 1a. It exhibits a kagome-like lattice, similar to bis(dithiolato)nickel ($\text{Ni}_3\text{C}_{12}\text{S}_{12}$)^{25,26} and bis(diimino)nickel ($\text{Ni}_3\text{C}_{12}(\text{NH})_{12}$)²⁷ monolayer. An interesting feature of

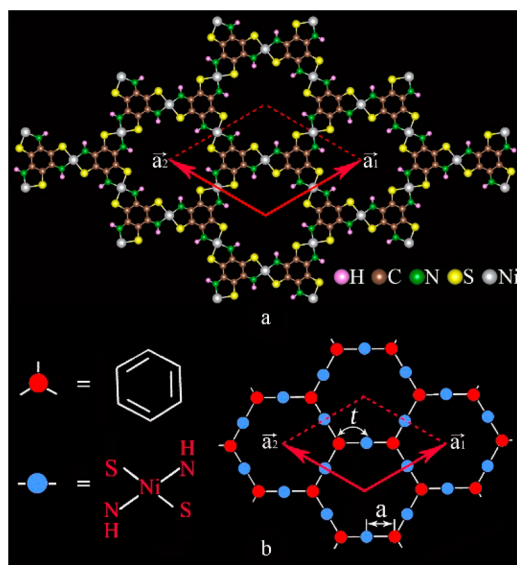


Figure 1. Schematic illustration of bis(iminothiolato)nickel monolayer. (a) Atomic structure; (b) line-centered honeycomb lattice. The unit cell is indicated by the red rhombic area with the two basis vectors \mathbf{a}_1 and \mathbf{a}_2 .

$\text{Ni}_3\text{C}_{12}(\text{NH})_6\text{S}_6$ distinct from the $\text{Ni}_3\text{C}_{12}\text{S}_{12}$ and $\text{Ni}_3\text{C}_{12}(\text{NH})_{12}$ is the bridging ligands with mixed ligating groups, which are expected to lead to new properties. The optimized lattice constant (the length of primitive basis vectors) is 13.89 Å, slightly shorter than that of $\text{Ni}_3\text{C}_{12}\text{S}_{12}$ (14.63 Å). The lengths of the C–C and C–N bonds are 1.427–1.433 and 1.342 Å, respectively, indicating the covalent bonding features. The stability of the bis(iminothiolato)nickel monolayer was also verified by the positive phonon spectrum, as shown in Figure S2.

Figure 2a gives the electronic band structure of bis(iminothiolato)nickel monolayer obtained by using HSE06

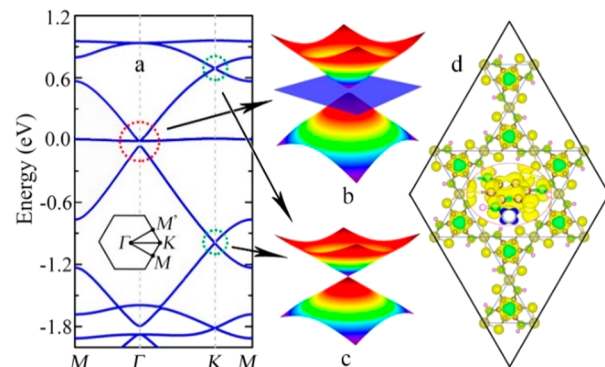


Figure 2. Electronic properties of bis(iminothiolato)nickel monolayer. (a) Band structure obtained from DFT calculations within the HSE06 functional. The energy at the Fermi level was set to zero. The local band profiles in the regions marked by red and blue circles are shown in panels b and c, which exhibit the features of pesudospin-1 Weyl semimetal (b) and pesudospin-1/2 Dirac semimetal (c). (d) The isosurfaces of the Kohn–Sham wave functions of the Kane-type bands nearest to Fermi level with an isovalue of 0.02 \AA^{-3} . The inset shows the enlarged view of the wave functions.

functional. Near the center of the Brillouin zone (BZ), the two conical bands and the nominally flat heavy hole band, as shown in Figure 2b, clearly remind us of the Kane model.^{14,15} The flat band is nearly dispersionless with a width of only 23 meV. The Fermi level crosses the meeting point of the upper cone and the flat band, whereas a small band gap of about 45 meV appears between the flat band and the lower cone. The semimetal features of the band structure are consistent with the good conductivity of the bis(iminothiolato)nickel nanosheet found in recent experiments.¹⁷ It is noteworthy that despite the Kane-type band alignment, Dirac cones also appear at the six corners (K and K') of the BZ in both valence and conduction bands, as shown in Figure 2c. The Fermi velocities of these conical bands (referred to as K-point Dirac cones) are $0.229 \times 10^6 \text{ m/s}$ (upper cone) and $0.444 \times 10^6 \text{ m/s}$ (lower cone), respectively, both of which are on the same order of that in graphene, $0.861 \times 10^6 \text{ m/s}$.

To reveal the origins of the conical bands and the flat band, we plotted the Kohn–Sham wavefunctions of these bands in Figure 2d and found that they come mainly from the p_z orbitals of C, N, S and Ni atoms together with the d_{xz} and d_{yz} orbitals of Ni. These features are in good consistence with the orbital-resolved electron density of states (see Supporting Information). The hybridization between the p_z orbitals of organic ligands and the d_{xz} and d_{yz} orbitals of the transition metal atoms leads to a π -conjugated 2D MOF with the Kane-type band alignment.

We then applied biaxial strain to tune the electronic band structure of the bis(iminothiolato)nickel monolayer. It was found that under tensile strain, the semimetallic feature (the touching of the upper conical band with the flat band) was preserved, whereas the band gap between the flat band and the lower conical band was enlarged, as shown in Figure 3.

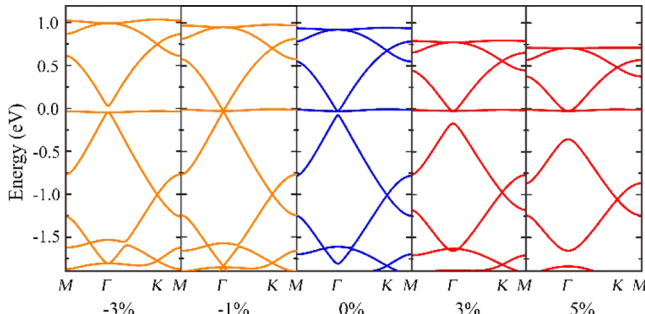


Figure 3. Strain effects of bis(iminothiolato)nickel monolayer. Electronic band structure evolution under equal-biaxial strain. HSE06 functional was employed without SOC. The energy at the Fermi level was set to zero.

Compressive strain, however, takes the lattice from a semimetal to a semiconductor. The flat band comes to touch the lower conical band, and a band gap appears between the upper conical band and the flat band. At a critical compressive strain of $\sim 1\%$, the upper and lower conical bands linearize and touch at a single point intersecting a flat band, showing the same dispersion as the pseudospin-1 Dirac–Weyl systems.^{12,13} The Fermi velocity of the conical bands at this critical strain is 0.540×10^6 m/s, which is also comparable to that of graphene.

The semimetal to semiconductor transition revealed in the bis(iminothiolato)nickel monolayer is quite similar to that discovered in $Hg_{1-x}Cd_xTe$.^{8,9} The major difference between the two cases is that, in the latter case, the electronic band structure was tuned intrinsically by the cadmium concentration, which is obviously irreversible. However, the strain-driven phase transition revealed in bis(iminothiolato)nickel monolayer offer a reversible approach to tune the electronic properties of Kane systems. From the experimental point of views, tensile and compressive stain can be stably applied to 2D materials by utilizing the thermal coefficient expansion mismatch between 2D materials and growth substrate, while preserving high material quality.²⁸ So, realization of the strain-driven phase transition in the bis(iminothiolato)nickel monolayer is plausible in the near future.

The Minimal Basis Line-Centered Honeycomb Lattice Model. Based on the orbital origins of the conical and flat bands, we implemented a model lattice to described the bis(iminothiolato)nickel monolayer. We treated the benzene rings as the vertexes of a honeycomb sublattice, while the remnant moieties ($Ni(NH)_2S_2$) that connect the benzene rings as the midpoints between two adjacent vertexes, as shown in Figure 1b. This LCH lattice can be regarded as a hybrid of a honeycomb sublattice and a kagome sublattice. The single-orbital TB Hamiltonian of the LCH lattice in the absence of spin-orbit coupling (SOC) can be written as

$$H(\vec{k}) = \begin{pmatrix} 0 & 0 & V_1 & V_2 & V_3 \\ 0 & 0 & V_1^* & V_2^* & V_3^* \\ V_1^* & V_1 & \epsilon & 0 & 0 \\ V_2^* & V_2 & 0 & \epsilon & 0 \\ V_3^* & V_3 & 0 & 0 & \epsilon \end{pmatrix}$$

with $V_1 = -te^{i(k_x\sqrt{3}a + k_ya)/2}$, $V_2 = -te^{i(k_x\sqrt{3}a - k_ya)/2}$, and $V_3 = -te^{-ik_ya}$. Here, a represents the distance between vertex and midpoint, as shown in Figure 1b, which is 4.01 \AA for the bis(iminothiolato)nickel monolayer. Only the electron hopping between adjacent sites with an amplitude of t ($t > 0$) were considered. The on-site energy difference between the kagome sublattice (midpoint) and the honeycomb sublattice (vertex) was set to ϵ , which reflects the charge transfer between the two subsystems. The TB Hamiltonian leads to the five energy spectra as

$$E_1 = \epsilon$$

$$E_{2,3} = \frac{1}{2} \times (\epsilon \pm \sqrt{\epsilon^2 + 4t^2(3 - |f(\vec{k})|)})$$

and

$$E_{4,5} = \frac{1}{2} \times (\epsilon \pm \sqrt{\epsilon^2 + 4t^2(3 + |f(\vec{k})|)})$$

with

$$|f(\vec{k})| = \sqrt{3 + 2 \cos(2\sqrt{3}k_xa) + 4 \cos(\sqrt{3}k_xa) \cos(3k_ya)}$$

The alignment of the flat band (E_1) and the conical bands (E_2 and E_3) is determined by the sign of ϵ , as shown in Figure 4. When $\epsilon > 0$, the flat band touches the upper conical band

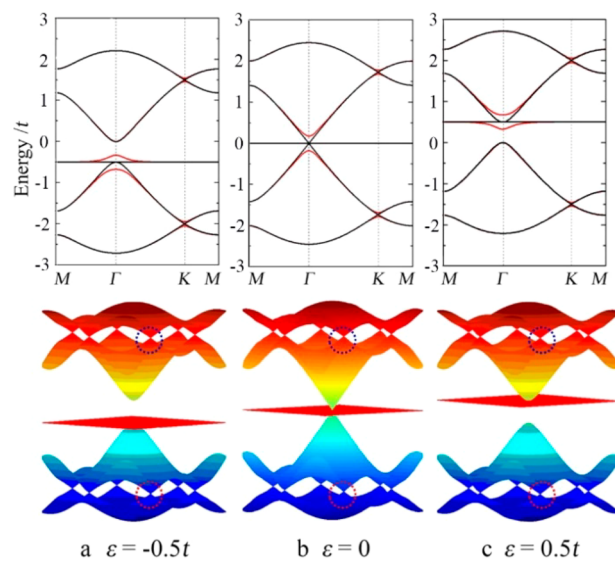


Figure 4. Tight-binding electronic band structures of the line-centered honeycomb lattice with different on-site energy difference ϵ . (Top) Band lines without (black lines) and with SOC (red lines) at $\epsilon = -0.5t$, 0 and $0.5t$. The SOC strength was set to $\lambda = 0.05t$. (Bottom) Band contours without SOC. The Dirac cones near the corners of the Brillouin zone are indicated by the dotted circles. The Fermi level resides between the upper conical band and the flat band, according to the electron counting rule.

(E_2) at a single point at the Γ point, while a band gap of ε appears between the flat band and the lower conical band (E_3). For a negative ε ; however, the flat band touches the lower conical band (E_3), and a band gap of $|\varepsilon|$ exists between the flat band and the upper conical band (E_2). At a critical value of $\varepsilon = 0$, the upper and lower conical bands linearize and touch at a single point intersecting the flat band. In this condition, the first three energy spectra near the Γ point become:

$$E_{1,2,3} = 0, \pm \hbar v_F |\vec{k}|, \quad \text{with } v_F = \sqrt{3} at/\hbar$$

Such an electronic band diagram is quite similar to that of the low-energy Kane model.^{11–13}

Validity of LCH Model in $Ni_3C_{12}(NH)_6S_6$. The electronic band structure evolution of the bis(iminothiolato)nickel monolayer obtained from first-principles is understandable in terms of the above TB model. At the equilibrium state, the midpoint has a higher on-site energy than the vertex of the LCH lattice due to the N and S atoms, which gain electrons from C atoms. A positive value of $\varepsilon = 45$ meV was therefore obtained from the energy gap between the two conical bands at the Γ point, leading to the semimetallic nature of the bis(iminothiolato)nickel monolayer. Compressive strain causes electron redistribution between C and S atoms. Our first-principles calculations showed that the Bader charges of the C atom connecting to S atom increases to 5.48e from 4.30e as a 3% compressive strain was applied. This is equivalent to the decrease of ε in the TB model. We therefore deduce that it is the charge redistribution induced by compressive strain that is responsible for the semimetallic-to-semiconductor phase transition of the bis(iminothiolato)nickel monolayer. In addition, from the Fermi velocity of the conical bands at the critical point, the hopping energy t was determined to be 0.51 eV by fitting the DFT bands. This value is much lower than that in graphene, ~ 2.7 eV¹, but the Fermi velocity remains comparable to graphene, because the lattice constant of the bis(iminothiolato)nickel monolayer is much longer than that of graphene. The TB bands using this parameter reproduce well the conical and flat bands obtained from DFT calculations, as shown in Figure S5 (Supporting Information). The validity of the above TB Hamiltonian also suggests that the Kane-type electronic band structure of the bis(iminothiolato)nickel monolayer is independent of the strong correlation from d electrons of the transition metal atoms, which was not taken into account in the TB model. Similar results have also been reported for other 2D MOFs where the strong d -electron correlation effects are not responsible for the kagome-type band structures.^{21–23}

We now turn to the band topology of the bis(iminothiolato)-nickel monolayer. First, we used the TB model of the LCH to reveal the topological nontriviality of the electronic band structure of bis(iminothiolato)nickel monolayer, by introducing an intrinsic SOC term into its Hamiltonian,

$$H_{\text{SO}} = i\lambda \sum_{\langle\langle i,j\rangle\rangle, \alpha, \beta} (\overrightarrow{d}_{i,j}^1 \times \overrightarrow{d}_{i,j}^2) \cdot \sigma_{\alpha, \beta} c_{i\alpha}^+ c_{j\beta}$$

where λ represents the amplitude for the next-nearest-neighbor (NNN) spin-orbit-induced interaction. $\overrightarrow{d}_{i,j}^1$ and $\overrightarrow{d}_{i,j}^2$ are the two-unit vectors along the nearest-neighbor bonds connecting site i to its NNN j and the term $v_{ij} = \overrightarrow{d}_{i,j}^1 \times \overrightarrow{d}_{i,j}^2 = \pm 1$. $\vec{\sigma}$ is the vector of Pauli spin matrices. The SOC term preserves the

time-reversal symmetry (TRS) and the translational symmetry of Hamiltonian and yield topologically nontrivial gaps (called SOC gap) at the degenerate points, as shown in Figure 4. The energy degeneracy between the conical band (upper band for $\varepsilon > 0$ and lower band for $\varepsilon < 0$) and the flat at the Γ point is lifted. This is consistent with the first-principles calculations. We have calculated the electronic band structure of bis(iminothiolato)nickel monolayer at the equilibrium state by using the HSE06 functional, and found that SOC opens a tiny band gap of 10.1 meV between the upper conical band and the flat band. According to the TB Hamiltonian, the magnitude of the band gap due to SOC equals $2\sqrt{3}\lambda$. In combination with the DFT calculations, the SOC strength in the bis(iminothiolato)nickel monolayer is determined to be $\lambda = 2.89$ meV.

The topological nontriviality of the SOC band gap can be verified from the nonzero Z_2 topological invariant. Several equivalent approaches are available for the Z_2 calculations. For the lattice with inversion symmetry, the method proposed by Fu and Kane²⁹ is most convenient, because the Z_2 topological invariant can be calculated from the parities of the electron wave functions at the time-reversal invariant momenta, without having to know about the global properties of the energy bands. We have calculated the Z_2 topological invariant by using this method and found that both first-principles calculations and TB model gave a nonzero topological invariant of $Z_2 = 1$ confirming the topological nontriviality of the SOC gap (for details see the Supporting Information).

A topologically nontrivial SOC gap is always accompanied by topologically protected gapless modes in the electronic band structures of nanoribbons. We calculated the electronic band structures of a LCH nanoribbon with two asymmetric edges, as shown in Figure 5, through numerical diagonalization of the

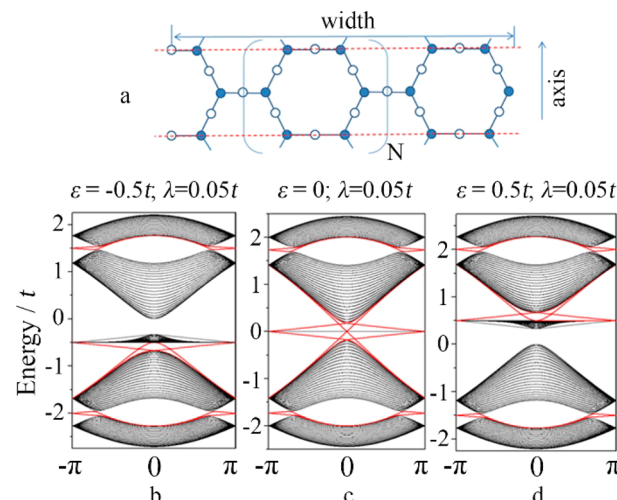


Figure 5. Intrinsic topological properties of LCH. (a) Geometry of a LCH nanoribbon with $N = 10$. (b–d) Electronic band structures with SOC for the nanoribbons. The topologically protected gapless states are indicated by the red lines.

Hamiltonian involving SOC. It is clear that an odd number of pairs of gapless modes appear along each edge of the nanoribbon, suggesting topological nontriviality of the SOC band gaps, consistent with the nonzero topological invariants. The above results show that, in the presence of SOC, compressive strain takes the bis(iminothiolato)nickel mono-

layer from a 2D Z_2 topological insulator ($\epsilon \geq 0$) to a normal semiconductor ($\epsilon < 0$). The small SOC band gap, however, makes the topological aspects work only at low temperatures.

It is noteworthy that the TB model not only reproduces the Kane-type spectra near the Γ point, but also gives the Dirac cones centered at the K and K' points in the valence and conduction band regions, as shown in Figure 2, Figure 4, and Figure S5. At the critical point ($\epsilon = 0$), the TB energy spectra near the K and K' points can be reduced to

$$E_{2,4} = E_{3,5} = \pm \hbar v_F^K |\vec{k}|, \quad \text{with} \quad v_F^K = (\sqrt{3}/2)at/\hbar$$

The parameters $t = 0.51$ eV and $a = 4.01$ Å that were used to fit the Kane-type dispersion, give a Fermi velocity of $v_F^K = 0.270 \times 10^6$ m/s. This value is very close to the DFT results: 0.233×10^6 m/s (upper cone) and 0.448×10^6 m/s (lower core), respectively. Additionally, in the absence of SOC, these K-point Dirac cones are robust against the strain with a ϵ -dependent

Fermi velocity $\tilde{v}_F^K = v_F^K / \sqrt{1 + \epsilon^2/(12t^2)}$ as shown in Figure 3 and Figure 4. The Fermi velocity decreases with the increase of $|\epsilon|$. This tendency agrees with the band structure evolution shown in Figure 3. To make it more clearly, we calculated the variation of on-site energy ϵ and the Fermi velocities of the upper and down K-point Dirac cones as a function of strain and plotted them in Figure S7. Obviously, with the increase of tensile strain, the on-site energy ϵ increases, and the Fermi velocities decrease. Our TB model gives the same trend. The deviation in magnitude between the TB and DFT data is related to the simplification of the TB model with the minimal basis where the atomic orbitals of the 2D MOF are reduced. It is interesting to see that, as the compressive strain exceeds 1%, ϵ changes sign, corresponding to the semimetallic-to-semiconductor transition. When SOC is switched on, these Dirac cones are gapped, as shown in Figure 4. According to the TB Hamiltonian, the band gap opened at K-point Dirac cones equals $\sqrt{3}\lambda$, which is about 5.05 meV for the bis(iminothiolato)nickel monolayer. The topological nontriviality of the SOC gaps at the K and K' points were confirmed by the nonzero Z_2 topological invariant and the topologically protected gapless modes in the electronic band structures of nanoribbons, as shown in Figure 5. The coexistence of Kane-type spectra and Dirac-type spectra in the bis(iminothiolato)nickel monolayer has never been reported in other materials, which will benefit the study of multi quasiparticle effects.

Finally, concerning the diversity of MOFs arising from different transition metal atoms and organic ligands, we also considered a similar structure by replacing the Ni of the bis(iminothiolato)nickel monolayer with Co. The electronic band structure of the bis(iminothiolato)cobalt monolayer is quite similar to that of the bis(iminothiolato)nickel monolayer, except for the electron spin-polarization due to Co atoms, as shown in Figure S8. The electron spin-polarization and half-metallicity of the bis(iminothiolato)cobalt monolayer offer additional ways of tuning the electronic properties of 2D Kane systems.

Our first-principles calculations demonstrated the recently synthesized 2D bis(iminothiolato)nickel monolayer is implementable for achieving a 2D massless Kane fermion, a new type of relativistic quasiparticles, thanks to the conical bands and the flat band near the Fermi level. Compressive strain takes the bis(iminothiolato)nickel monolayer from a semimetal to a semiconductor. At the critical value of ~1%, the upper and lower conical bands linearize and touch at a single point

intersecting a flat band, showing the same dispersion as the Kane model. By simplifying the bis(iminothiolato)nickel monolayer to a line-centered honeycomb lattice, we proposed a tight-binding Hamiltonian to reproduce the band structure evolution under strain. Our TB Hamiltonian revealed that it is the charge redistribution induced by strain that is responsible for the semimetal to semiconductor transition. In the presence of intrinsic spin-orbit coupling, the touching point between the conical and flat bands is gapped. At equilibrium state, bis(iminothiolato)nickel monolayer is a 2D topological insulator with a bulk band gap of 10.1 meV. As the compressive strain exceeds the critical value of ~1%, it becomes a normal semiconductor. Compared with the 3D massless Kane fermion achieved in $Hg_{1-x}Cd_xTe$ through fine control of cadmium concentration, the strain-driven phase transition revealed in bis(iminothiolato)nickel monolayer offers a reversible approach to tune the electronic properties of Kane systems.

COMPUTATIONAL METHODS

Our DFT calculations for stability, band structures and topological properties of the 2D MOF lattice were carried out in the framework of Perdew–Burke–Ernzerhof (PBE)-type generalized gradient approximation (GGA) functional³⁰ using VASP package.^{31,32} All self-consistent calculations were performed with a plane-wave cutoff of 520 eV on $9 \times 9 \times 1$ Monkhorst-Park k -point mesh on primitive cells with a vacuum space about 20 Å to avoid interaction between adjacent images. For structural relaxation, all the atoms are fully relaxed without any symmetry restriction until the residual forces on each atom are smaller than 0.01 eV/Å. To avoid the self-interaction errors of the PBE functional,³³ the hybrid functional in the form of HSE06³⁴ was adopted in the electronic band structure calculations.

ASSOCIATED CONTENT

Supporting Information

The Supporting Information is available free of charge on the ACS Publications website at DOI: [10.1021/acs.jpclett.7b03021](https://doi.org/10.1021/acs.jpclett.7b03021).

Band structures of bulk materials; geometry details of bis(iminothiolato)nickel monolayer; orbital-resolved electron density; comparison of the band lines obtained from DFT and TB model; Z_2 topological invariant calculations; variations of ϵ and Fermi velocity in response to external strain; spin-resolved electronic band structure of bis(iminothiolato)cobalt monolayer (PDF)

AUTHOR INFORMATION

Corresponding Authors

*E-mail: zmw@sdu.edu.cn (M.Z.).

*E-mail: phyfp@nus.edu.sg (Y.F.).

ORCID

Aizhu Wang: [0000-0003-2297-5426](https://orcid.org/0000-0003-2297-5426)

Mingwen Zhao: [0000-0002-7583-9682](https://orcid.org/0000-0002-7583-9682)

Feng Liu: [0000-0002-3701-8058](https://orcid.org/0000-0002-3701-8058)

Author Contributions

A.Z.W. performed DFT calculations and contributed to data interpretation and writing the manuscript. X.R.Z. solved the TB Hamiltonian and contributed to the TB calculations. M.W.Z. designed the study, proposed the TB model, and contributed to the data interpretation and writing the manuscript. X.M.Z.

conducted the edge state calculations. Y.P.F. and L.F. contributed to the data interpretation and writing the manuscript. All authors have given approval to the final version of the manuscript.

Notes

The authors declare no competing financial interest.

ACKNOWLEDGMENTS

A.Z.W. greatly appreciates the ASTAT Topological Insulator fund of Singapore (No. 1527400026). M.W.Z. thanks the support from the National Natural Science Foundation of China (Nos. 21433006 and 11774201). F.L. acknowledges support by the United States Department of Energy Basic Energy Sciences (Grant No. DE-FG02-04ER46148). The computational resources were provided by the Centre for Advanced 2D Materials of the National University of Singapore in Singapore and the National Super Computing Centre in Jinan.

REFERENCES

- (1) Castro Neto, A. H.; Guinea, F.; Peres, N. M.; Novoselov, K. S.; Geim, A. K. The electronic properties of graphene. *Rev. Mod. Phys.* **2009**, *81* (1), 109–162.
- (2) Hasan, M. Z.; Kane, C. L. Colloquium: topological insulators. *Rev. Mod. Phys.* **2010**, *82* (4), 3045–3067.
- (3) Qi, X.-L.; Zhang, S.-C. Topological insulators and superconductors. *Rev. Mod. Phys.* **2011**, *83* (4), 1057–1110.
- (4) Dziawa, P.; Kowalski, B.; Dybko, K.; Buczko, R.; Szczerbakow, A.; Szot, M.; Łusakowska, E.; Balasubramanian, T.; Wojek, B. M.; Berntsen, M.; et al. Topological crystalline insulator states in $Pb_{(1-x)}Sn_xSe$. *Nat. Mater.* **2012**, *11*, 1023–1027.
- (5) Liu, Z.; Jiang, J.; Zhou, B.; Wang, Z.; Zhang, Y.; Weng, H.; Prabhakaran, D.; Mo, S.; Peng, H.; Dudin, P.; et al. A stable three-dimensional topological Dirac semimetal Cd_3As_2 . *Nat. Mater.* **2014**, *13* (7), 677–681.
- (6) Lv, B.; Xu, N.; Weng, H.; Ma, J.; Richard, P.; Huang, X.; Zhao, L.; Chen, G.; Matt, C.; Bisti, F.; et al. Observation of Weyl nodes in TaAs. *Nat. Phys.* **2015**, *11*, 724–727.
- (7) Yang, L.; Liu, Z.; Sun, Y.; Peng, H.; Yang, H.; Zhang, T.; Zhou, B.; Zhang, Y.; Guo, Y.; Rahn, M.; et al. Weyl semimetal phase in the non-centrosymmetric compound TaAs. *Nat. Phys.* **2015**, *11*, 728–732.
- (8) Orlita, M.; Basko, D.; Zholudev, M.; Teppe, F.; Knap, W.; Gavrilenko, V.; Mikhailov, N.; Dvoretskii, S.; Neugebauer, P.; Faugeras, C.; et al. Observation of three-dimensional massless Kane fermions in a zinc-blende crystal. *Nat. Phys.* **2014**, *10*, 233–238.
- (9) Teppe, F.; Marcinkiewicz, M.; Krishtopenko, S.; Ruffenach, S.; Consejo, C.; Kadykov, A.; Desrat, W.; But, D.; Knap, W.; Ludwig, J.; et al. Temperature-driven massless Kane fermions in HgCdTe crystals. *Nat. Commun.* **2016**, *7*, 12576.
- (10) Akrap, A.; Hakl, M.; Tchoumakov, S.; Crassee, I.; Kuba, J.; Goerbig, M.; Homes, C.; Caha, O.; Novák, J.; Teppe, F.; et al. Magneto-Optical Signature of Massless Kane Electrons in Cd_3As_2 . *Phys. Rev. Lett.* **2016**, *117* (13), 136401.
- (11) Kane, E. O. Band structure of indium antimonide. *J. Phys. Chem. Solids* **1957**, *1* (4), 249–261.
- (12) Burkov, A.; Balents, L. Weyl semimetal in a topological insulator multilayer. *Phys. Rev. Lett.* **2011**, *107* (12), 127205.
- (13) Delplace, P.; Li, J.; Carpentier, D. Topological Weyl semi-metal from a lattice model. *EPL* **2012**, *97* (6), 67004.
- (14) Malcolm, J. D.; Nicol, E. J. Magneto-optics of massless Kane fermions: Role of the flat band and unusual Berry phase. *Phys. Rev. B: Condens. Matter Mater. Phys.* **2015**, *92* (3), 035118.
- (15) Malcolm, J. D.; Nicol, E. J. Analytic evaluation of Kane fermion magneto-optics in two and three dimensions. *Phys. Rev. B: Condens. Matter Mater. Phys.* **2016**, *94* (22), 224305.
- (16) Raoux, A.; Morigi, M.; Fuchs, J.-N.; Piéchon, F.; Montambaux, G. From Dia-to paramagnetic orbital susceptibility of massless fermions. *Phys. Rev. Lett.* **2014**, *112* (2), 026402.
- (17) Sun, X.; Wu, K.-H.; Sakamoto, R.; Kusamoto, T.; Maeda, H.; Nishihara, H. Conducting π -Conjugated Bis (iminothiolato) nickel Nanosheet. *Chem. Lett.* **2017**, *46* (8), 1072–1075.
- (18) Rosi, N. L.; Eckert, J.; Eddaoudi, M.; Vodak, D. T.; Kim, J.; O'keeffe, M.; Yaghi, O. M. Hydrogen storage in microporous metal-organic frameworks. *Science* **2003**, *300* (5622), 1127–1129.
- (19) Long, J. R.; Yaghi, O. M. The pervasive chemistry of metal-organic frameworks. *Chem. Soc. Rev.* **2009**, *38* (5), 1213–1214.
- (20) James, S. L. Metal-organic frameworks. *Chem. Soc. Rev.* **2003**, *32* (5), 276–288.
- (21) Wang, Z.; Liu, Z.; Liu, F. Quantum anomalous Hall effect in 2D organic topological insulators. *Phys. Rev. Lett.* **2013**, *110* (19), 196801.
- (22) Wang, Z.; Su, N.; Liu, F. Prediction of a two-dimensional organic topological insulator. *Nano Lett.* **2013**, *13* (6), 2842–2845.
- (23) Zhao, M.; Wang, A.; Zhang, X. Half-metallicity of a kagome spin lattice: the case of a manganese bis-dithiolene monolayer. *Nanoscale* **2013**, *5* (21), 10404–10408.
- (24) Wang, A.; Zhang, X.; Feng, Y. P.; Zhao, M. Chern insulator and Chern half-metal states in the two-dimensional spin-gapless semiconductor $Mn_2C_6S_{12}$. *J. Phys. Chem. Lett.* **2017**, *8* (16), 3770–3775.
- (25) Kambe, T.; Sakamoto, R.; Hoshiko, K.; Takada, K.; Miyachi, M.; Ryu, J.-H.; Sasaki, S.; Kim, J.; Nakazato, K.; Takata, M.; et al. π -Conjugated nickel bis (dithiolene) complex nanosheet. *J. Am. Chem. Soc.* **2013**, *135* (7), 2462–2465.
- (26) Kambe, T.; Sakamoto, R.; Kusamoto, T.; Pal, T.; Fukui, N.; Hoshiko, K.; Shimojima, T.; Wang, Z.; Hirahara, T.; Ishizaka, K.; et al. Redox control and high conductivity of nickel bis (dithiolene) complex π -nanosheet: a potential organic two-dimensional topological insulator. *J. Am. Chem. Soc.* **2014**, *136* (41), 14357–14360.
- (27) Lahiri, N.; Lotfizadeh, N.; Tsuchikawa, R.; Deshpande, V. V.; Louie, J. Hexaaminobenzene as a building block for a Family of 2D Coordination Polymers. *J. Am. Chem. Soc.* **2017**, *139* (1), 19–22.
- (28) Ahn, G. H.; Amani, M.; Rasool, H.; Lien, D.-H.; Mastandrea, J. P.; Ager, J. W., III; Dubey, M.; Chrzan, D. C.; Minor, A. M.; Javey, A. Strain-engineered growth of two-dimensional materials. *Nat. Commun.* **2017**, *8*, 608.
- (29) Fu, L.; Kane, C. L. Topological insulators with inversion symmetry. *Phys. Rev. B: Condens. Matter Mater. Phys.* **2007**, *76* (4), 045302.
- (30) Perdew, J. P.; Burke, K.; Ernzerhof, M. Generalized gradient approximation made simple. *Phys. Rev. Lett.* **1996**, *77* (18), 3865.
- (31) Kresse, G.; Hafner, J. Norm-conserving and ultrasoft pseudopotentials for first-row and transition elements. *J. Phys.: Condens. Matter* **1994**, *6* (40), 8245.
- (32) Kresse, G.; Joubert, D. From ultrasoft pseudopotentials to the projector augmented-wave method. *Phys. Rev. B: Condens. Matter Mater. Phys.* **1999**, *59* (3), 1758.
- (33) Perdew, J. P. Density functional theory and the band gap problem. *Int. J. Quantum Chem.* **1986**, *30* (3), 451–451.
- (34) Heyd, J.; Scuseria, G. E.; Ernzerhof, M. Hybrid functionals based on a screened Coulomb potential. *J. Chem. Phys.* **2003**, *118* (18), 8207–8215.